International Journal of Multiphase Flow 205 (2026) 105971

Contents lists available at ScienceDirect

International Journal of Multiphase Flow

journal homepage: www.elsevier.com/locate/ijmulflow

Research Paper

# A sub-grid-scale model for polydisperse bubbly flows with heat and mass transfer

Anand Radhakrishnan [a], Spencer H. Bryngelson [b,c,*]

[a] School of Computational Science & Engineering, Georgia Institute of Technology, Atlanta, GA 30332, USA
[b] Walker Department of Mechanical Engineering, The University of Texas at Austin, Austin, TX 78712, USA
[c] Oden Institute for Computational Engineering and Sciences, The University of Texas at Austin, Austin, TX 78712, USA

ARTICLE INFO

Dataset link: github.com/MFlowCode/MFC, 10.5281/zenodo.21590440

*Keywords:*
Bubbly flow
Population balance
Quadrature-based moment methods
Sub-grid-scale modeling
Heat and mass transfer
Compressible multiphase flow

ABSTRACT

Ensemble-averaged models of polydisperse bubbly flows require statistics of the evolving bubble population. Prior quadrature-based moment formulations close bubble pressure with a polytropic relation that omits heat and mass transfer at the bubble wall. We couple the constant-transfer equations for bubble pressure and vapor mass to a conditional hyperbolic quadrature method of moments. Second-order conditional inversion produces four joint radius–radial-velocity nodes per equilibrium-radius bin. Bubble pressure and vapor mass are advanced at each node. These node values close the ensemble-averaged flow equations, and the transport keeps the six moments per bin of the polytropic formulation. We implement the model in the open-source solver MFC. For a harmonically forced population, the mean radius agrees with Monte Carlo calculations with a 0.81 % root-mean-square (RMS) relative error. For an acoustically excited bubble screen, 51 equilibrium-radius bins give a center pressure within 0.026 % of a 91-bin reference, and this error increases with the width of the equilibrium-radius distribution. The constant-transfer closure reduces the late-time root-mean-square pressure fluctuation by a factor of 9.5 compared to the polytropic closure. For a three-dimensional bubble screen, the Euler–Euler pressure at the screen center matches the mean of 40 volume-averaged Euler–Lagrange realizations with a 1.5% RMS relative error.

## 1. Introduction

In bubbly flows, the bubbles span a wide range of length and time scales, so resolved simulations are limited to small problems. Sub-grid-scale models reduce the cost by modeling the bubbles statistically. Euler–Lagrange simulations track each dispersed-phase particle (Maeda and Colonius, 2018; Vaca-Revelo et al., 2026), though their cost scales with the number of bubbles. Thus, we treat the dispersed phase in an Eulerian frame. Eulerian two-fluid models reach larger systems, such as bubble columns (Schlegel et al., 2025). The bubbles in such systems are polydisperse, with sizes set by formation processes such as detachment in liquid cross-flow (Vorobyev et al., 2025). Colonius et al. (2008) showed that, under impulsive forcing, the moments of dilute bubble populations rapidly approach a statistical equilibrium and can be computed via period-averaged bubble dynamics. The method of classes (MOC) employs ensemble phase averaging (Zhang and Prosperetti, 1994; Bryngelson et al., 2019) to couple the dispersed and resolved phases. The polydisperse bubble population is initialized using a log-normal distribution for the equilibrium radii. Averages of the bubble variables are then weighted sums over the bins of this distribution, with weights from Simpson's rule. The method of classes is inexpensive compared to Lagrangian methods, though only the equilibrium radius $R_0$ is random, and the other internal variables are fixed at each $R_0$. Representing the spread of bubble radius and radial velocity at each $R_0$ requires treating these variables as random.

The internal bubble variables at each $R_0$ are modeled using the population balance equation (PBE). PBEs model the probability density of the dispersed phase (Vanni, 2000). The PBE uses the bubble radius and radial velocity as internal variables and is solved via the method of moments (MOM) (McGraw, 1997). The MOM uses quadrature nodes to approximate unclosed high-order moments arising in the coupled flow equations (McGraw, 1997; Fox et al., 2018). PBE-based models also represent soot formation in combustion (Mueller et al., 2009) and aerosol sprays (Sibra et al., 2017). We use a PBE-based method to represent the polydisperse bubbly phase (Fox, 2008). Quadrature-based moment methods (QBMM) represent polydisperse distributions in an Eulerian frame and have been applied to bubbly flows and multivariate turbulent gas–liquid systems (Heylmun et al., 2019; Buffo et al., 2013).

* Corresponding author.
*E-mail address:* shb@utexas.edu (S.H. Bryngelson).

https://doi.org/10.1016/j.ijmultiphaseflow.2026.105971
Received 29 July 2026; Received in revised form 27 September 2026; Accepted 19 October 2026
0301-9322/© 2026 Elsevier Ltd. All rights are reserved, including those for text and data mining, AI training, and similar technologies.

Previous PBE-based bubble models use the radius $R$, radial velocity $\dot{R}$, and equilibrium radius $R_0$ as internal variables. The bubble radii and velocities of the polydisperse bubble population are initialized using a Gaussian distribution with means $R_0$ and 0, respectively. A polytropic assumption models the bubble pressure $p_b$ as a function of $R$ and $R_0$. However, heat and mass transfer at the bubble wall require a model such as the constant-transfer model (Preston et al., 2007). Such models expand the set of relevant internal variables to include the bubble pressure $p_b$ and the vapor mass $m_v$. Treating $p_b$ and $m_v$ as independent PBE coordinates requires mixed moments in $(R, \dot{R}, p_b, m_v)$. For example, evaluating $\overline{R^3 p_{bw}}$ with these coordinates requires 70 moments per $R_0$ bin, compared to 6 for the polytropic formulation. A polytropic relation avoids these moments but omits heat and vapor-mass transfer.

The model extends the polytropic formulation of Bryngelson et al. (2023). Instead of adding PBE coordinates, we advance $p_b$ and $m_v$ via the constant-transfer equations at the $(R, \dot{R})$ quadrature nodes of each equilibrium-radius bin. We use the CHyQMOM inversion of Fox et al. (2018) and the constant-transfer equations of Preston et al. (2007). The node values of $p_b$ and $m_v$ are initialized at the CHyQMOM nodes and advanced with the radius abscissae. They then close the ensemble pressure term. Since $p_b$ and $m_v$ are not PBE coordinates, the transport system keeps the six moments per $R_0$ bin of the polytropic formulation.

We implement the model in MFC (Bryngelson et al., 2021; Radhakrishnan et al., 2024) and compare the node evolution and mean bubble variables with Monte Carlo calculations for a harmonically forced population. We then consider an acoustically excited bubble screen and measure how the number of equilibrium-radius bins and the initial distributions affect the closure error. We compare the resulting pressure response with the polytropic closure and, in three dimensions, with the mean of 40 volume-averaged Euler–Lagrange realizations (Vaca-Revelo et al., 2026).

## 2. Model formulation

### 2.1. Compressible flow equations

The governing equations for the liquid phase follow from the mixture-averaged compressible flow equations as

$$\begin{aligned} \frac{\partial \rho}{\partial t} + \nabla \cdot (\rho \boldsymbol{u}) &= 0, \\ \frac{\partial \rho \boldsymbol{u}}{\partial t} + \nabla \cdot (\rho \boldsymbol{u}\boldsymbol{u} + p\boldsymbol{I}) &= 0, \\ \frac{\partial E}{\partial t} + \nabla \cdot [(E+p)\boldsymbol{u}] &= 0, \end{aligned} \tag{1}$$

where $\rho$, $\boldsymbol{u}$, $p$, and $E$ are the density, velocity vector, pressure, and total energy. The density of the dispersed phase is considered negligible compared to the liquid phase. The liquid and dispersed phases share one velocity (no slip). The contribution of the dispersed phase to the flow equations in (1) is modeled via ensemble phase averaging.

### 2.2. Ensemble phase averaging

We use ensemble phase-averaged equations from prior work (Zhang and Prosperetti, 1994; Ando et al., 2011; Bryngelson et al., 2019). We use $\alpha \equiv \alpha_b$ for the bubble void fraction, so that $1-\alpha = \alpha_l$ is the liquid volume fraction in (2)–(6). The flow is dilute, with $\alpha_b \ll 1$. The bubbles are represented statistically via random variables $R$, $\dot{R}$, and $R_0$ for the instantaneous bubble radius, its time derivative, and the equilibrium bubble radius. The mixture-averaged pressure field is computed as

$$p(\boldsymbol{x}, t) = (1-\alpha) p_l + \alpha \left( \frac{\overline{R^3 p_{bw}}}{\overline{R^3}} - \rho \frac{\overline{R^3 \dot{R}^2}}{\overline{R^3}} \right), \tag{2}$$

where $p_{bw}$ is the associated bubble wall pressure and $p_l(\boldsymbol{x}, t)$ is the liquid pressure according to the stiffened-gas equation of state (Menikoff and Plohr, 1989),

$$p_l + \gamma_l \pi_{\infty,l} = \frac{\gamma_l - 1}{1-\alpha} \left( E - \frac{1}{2} \rho \boldsymbol{u}^2 \right), \tag{3}$$

where $\gamma_l$ is the specific heat ratio of the liquid and $\pi_{\infty,l}$ is the liquid stiffness. The energy equation in (1) conserves the mixture total energy. The wall heat and vapor fluxes in (18) update the bubble pressure and composition, which enter the mixture pressure in (2). The carrier-liquid equations receive no corresponding mass or heat sources. The finite-volume update does not conserve the thermal energy and phase mass exchanged by evaporation and condensation, which are neglected for $\alpha_b \ll 1$. Larger void fractions or strong phase change require conservative interphase source terms and a model of the liquid thermal boundary layer. The bubble number density per unit volume $n(\boldsymbol{x}, t)$ is conserved as

$$\frac{\partial n}{\partial t} + \nabla \cdot (n \boldsymbol{u}) = 0. \tag{4}$$

For the spherical bubbles considered here, $n$ is related to the void fraction $\alpha$ via

$$\alpha(\boldsymbol{x}, t) = \frac{4}{3} \pi \overline{R^3} n(\boldsymbol{x}, t), \tag{5}$$

and thus the void fraction $\alpha(\boldsymbol{x}, t)$ transports as

$$\frac{\partial \alpha}{\partial t} + \nabla \cdot (\alpha \boldsymbol{u}) = \alpha \nabla \cdot \boldsymbol{u} + 3\alpha \frac{\overline{R^2 \dot{R}}}{\overline{R^3}}, \tag{6}$$

where the right-hand side represents the change in void fraction due to bubble growth and collapse.

The over-barred terms appearing in (2), (5), and (6),

$$\overline{R^3 \dot{R}^2},\ \overline{R^3},\ \overline{R^2 \dot{R}},\ \text{and}\ \overline{R^3 p_{bw}} \tag{7}$$

denote average quantities of the bubble dispersion. The moments $\mu_{lmn}$ are averages over the probability density function (PDF) $f(R, \dot{R}, R_0)$,

$$\mu_{lmn} = \overline{R^l \dot{R}^m R_0^n} = \int_\Omega R^l \dot{R}^m R_0^n f(R, \dot{R}, R_0)\, \mathrm{d}R \mathrm{d}\dot{R} \mathrm{d}R_0. \tag{8}$$

For the method of classes, $R$ and $\dot{R}$ are fixed at each $R_0$, so $f(R, \dot{R}, R_0)$ reduces to $f(R_0)$, a log-normal distribution with mean $\mu_{R_0} = 1$ and standard deviation $\sigma_{R_0}$. Since $R_0$ does not change in time, $f(R_0)$ is fixed. The integral (8) is computed via Simpson's rule over $n_b$ bins in $R_0$.

### 2.3. Population balance formulation and inversion

We follow the method-of-moments formulation of Bryngelson et al. (2023). Without coalescence or breakup, the conditional probability density function $f(R, \dot{R}|R_0)$ satisfies the PBE (Vanni, 2000)

$$\frac{\partial f}{\partial t} + \frac{\partial}{\partial R}(f\dot{R}) + \frac{\partial}{\partial \dot{R}}(f\ddot{R}) = 0 \tag{9}$$

Fig. 1 illustrates the PBE-based approach.

The evolution of the raw moments $\vec{\boldsymbol{\mu}}$ is then obtained by integrating the PBE. The set of transport equations for $\vec{\boldsymbol{\mu}}$ is

$$\frac{\partial n \vec{\boldsymbol{\mu}}}{\partial t} + \nabla \cdot (n \vec{\boldsymbol{\mu}} \boldsymbol{u}) = n \dot{\vec{\boldsymbol{\mu}}} = n \vec{\boldsymbol{g}} \tag{10}$$

where

$$g_{lmn} = l \mu_{l-1,m+1,n} + m \iiint_\Omega \ddot{R} R^l \dot{R}^{m-1} R_0^n f(R, \dot{R}, R_0)\, \mathrm{d}R \mathrm{d}\dot{R} \mathrm{d}R_0 \tag{11}$$

and $\Omega = \Omega_R \times \Omega_{\dot{R}} \times \Omega_{R_0} = (0, \infty) \times (-\infty, \infty) \times (0, \infty)$ (Bryngelson et al., 2020). The integral is computed via quadrature nodes obtained by a conditional hyperbolic inversion procedure (Fox et al., 2018). The bubble dynamics $\ddot{R}$ is described in Section 2.4. The PDF $f(R, \dot{R}, R_0)$ is then related to the conditional PDF via

$$f(R, \dot{R}, R_0) = f(R, \dot{R}|R_0) f(R_0), \tag{12}$$

and the raw moments are obtained as

$$\mu_{lmn} \equiv \int_{\Omega_{R_0}} f(R_0) R_0^n \mu_{lm}(R_0)\, \mathrm{d}R_0 \approx \sum_{i=1}^{n_b} w_i \widehat{R}_{0,i}^n\, \mu_{lm}(\widehat{R}_{0,i}), \tag{13}$$

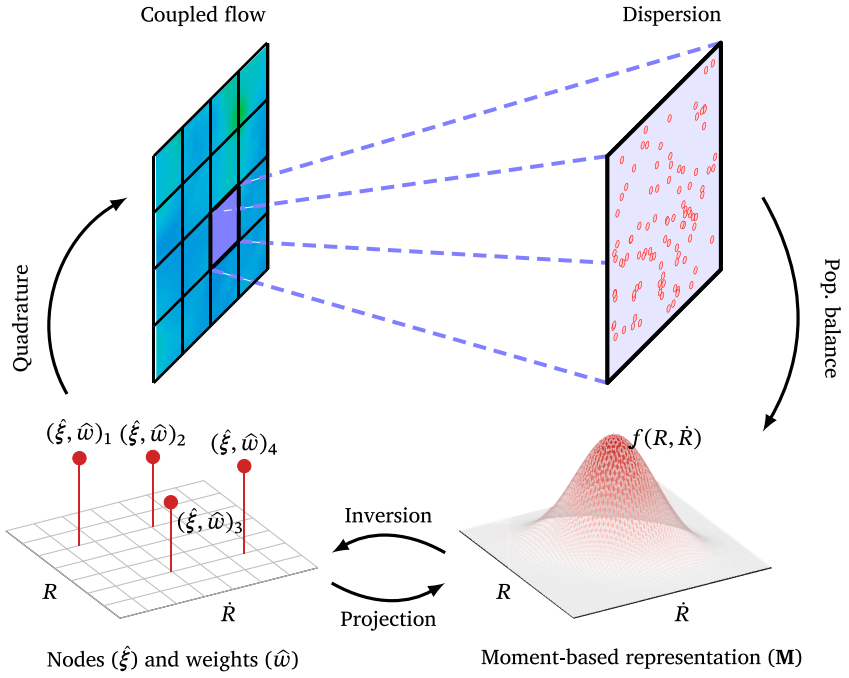



**Fig. 1.** Schematic of the moment method.
*Source:* Adapted from Bryngelson et al. (2020) with author permission.

where $n_b$ is the number of $R_0$ bins. The quadrature rule weights and nodes for $R_0$ are obtained through the same procedure as the method of classes. The $R_0$-conditioned moments $\mu_{lm}$ are then given by

$$\mu_{lm}(\widehat{R}_{0,i}) \equiv \iint_{\Omega_{R,\dot{R}}} f(R,\dot{R}|\widehat{R}_{0,i}) R^l \dot{R}^m \,\mathrm{d}R\mathrm{d}\dot{R} \approx \sum_{j=1}^{N_R}\sum_{k=1}^{N_{\dot{R}}} \left[\widehat{w}_{j,k}\widehat{R}_j^l \widehat{\dot{R}}_k^m\right]_{\widehat{R}_{0,i}}. \tag{14}$$

The conditional quadrature method (Yuan and Fox, 2011; Patel et al., 2019) sets the transported moments and the node counts $N_R$ and $N_{\dot{R}}$ in (14). The CHyQMOM algorithm is described in Fox et al. (2018). Substituting (14) into (13) gives

$$\mu_{lmn} = \sum_{i=1}^{n_b} w_i \widehat{R}_{0,i}^n \sum_{j=1}^{N_R}\sum_{k=1}^{N_{\dot{R}}} \left[\widehat{w}_{j,k}\widehat{R}_j^l \widehat{\dot{R}}_k^m\right]_{\widehat{R}_{0,i}}. \tag{15}$$

These moments evaluate the right-hand side of the moment evolution Eq. (10) and the ensemble-phase averaged terms (7).

### 2.4. Bubble dynamics model

We model the bubble's radial dynamics with the Keller–Miksis equation, the compressible form of the Rayleigh–Plesset equation (Plesset and Prosperetti, 1977). This model assumes spherical bubbles filled with a gas–vapor mixture. The Keller–Miksis equation is

$$R\ddot{R}\left(1-\frac{\dot{R}}{c_l}\right) + \frac{3}{2}\dot{R}^2\left(1-\frac{\dot{R}}{3c_l}\right) = \frac{p_{bw}-p_l}{\rho_l}\left(1+\frac{\dot{R}}{c_l}\right) + \frac{R\,\dot{p}_{bw}}{\rho_l c_l}, \tag{16}$$

which is nondimensionalized by the reference bubble size $R_{0,\mathrm{ref}}$, liquid pressure $p_0$, and density $\rho_0$. The radiation term omits the time derivative of the liquid pressure $p_l$, since the bubble radius is much smaller than the acoustic wavelength. For $\dot{R} \ll c_l$, where $c_l$ is the liquid speed of sound, (16) reduces to the Rayleigh–Plesset equation. Here, $\rho_l$ is the liquid density, and the bubble wall pressure $p_{bw}$ is given as

$$p_{bw} = p_b - \frac{4\mu_l\dot{R}}{R} - \frac{2\sigma_l}{R} \tag{17}$$

where $p_b$ is the internal bubble pressure, and $\mu_l$ and $\sigma_l$ are the dynamic viscosity and surface tension of the liquid. The evolution of $p_b$ follows (Preston et al., 2007)

$$\begin{aligned} \dot{m}_v &= \frac{4\pi R^2 D\rho_{bw}}{1-\chi_{vw}}\frac{\partial\chi_{vw}}{\partial r}\Big|_{r=R}, \\ \dot{p}_b &= \frac{3\gamma_b}{R}\left(-\dot{R}p_b + R_v T_{bw}\frac{\dot{m}_v}{4\pi R^2} + \frac{\gamma_b-1}{\gamma_b}k_{bw}\frac{\partial T}{\partial r}\Big|_{r=R}\right), \end{aligned} \tag{18}$$

where $\chi_{vw}$, $k_{bw}$, $\rho_{bw}$, and $T_{bw}$ are the vapor mass fraction, thermal conductivity, density, and temperature at the bubble wall. Here, $D$ is the binary diffusion coefficient, $R_v$ is the gas constant, and $\gamma_b$ is the specific heat ratio. The bubble wall closures in (18) are defined in Preston et al. (2007). These closures approximate the wall gradients of temperature and vapor mass fraction with reduced-order relations. They assume a spherical bubble, continuum transport, and boundary layers that the constant-transfer approximation can represent. Thermal interactions between neighboring bubbles through the liquid are not modeled. The regime is characterized by the radial Reynolds, Weber, thermal Péclet, and mass Péclet numbers,

$$\mathrm{Re}_R = \frac{\rho_l R|\dot{R}|}{\mu_l}, \quad \mathrm{We}_R = \frac{\rho_l R\dot{R}^2}{\sigma_l}, \quad \mathrm{Pe}_T = \frac{R|\dot{R}|}{a_g}, \quad \mathrm{Pe}_m = \frac{R|\dot{R}|}{D}, \tag{19}$$

where $a_g$ is the gas-mixture thermal diffusivity. The thermal and mass Fourier numbers are $\mathrm{Fo}_T = a_g\tau_d/R^2$ and $\mathrm{Fo}_m = D\tau_d/R^2$, where $\tau_d$ is a time scale of the bubble dynamics. Tables 1 and 5 list their ranges. The closure does not treat violent collapse, bubble deformation, or overlapping boundary layers.

### 2.5. Coupling the constant-transfer model to the method of moments

The conditional moments $\mu_{lm}(\widehat{R}_{0,i})$ are truncated at second order, $l+m \le 2$. Initializing these moments requires the first- and second-order moments of the initial distribution. A joint normal distribution supplies them, with means $\mu_R$ and $\mu_{\dot{R}}$, standard deviations $\sigma_R$ and $\sigma_{\dot{R}}$, and a correlation coefficient $\rho_{R\dot{R}}$ at each bin $\widehat{R}_{0,i}$. A two-node inversion of

the radius moments is followed by a two-node inversion of the velocity moments conditioned on each radius node. This gives $N_R N_{\dot{R}} = 2{\times}2 = 4$ joint nodes, shown in Fig. 1. For the normalized second-order moment set used here, the hyperbolic construction assigns equal joint weights $\hat{\omega}_{j,i} = 1/4$. For a realizable moment vector, (21) and (22) reproduce $\mu_{00}$, both first-order moments, and all three second-order moments to round-off. Evaluating $\overline{R^3 p_{bw}}$ in (2) requires the statistics of the bubble pressure $p_b$. The ODEs for $p_b$ and $m_v$ in (18) are evolved at the $(R, \dot{R})$ quadrature nodes. The moment set $\mu_{lm}(\hat{R}_{0,i})$ is initialized as

$$\begin{gathered}\mu_{0,0}(\hat{R}_{0,i}) = 1, \qquad \mu_{1,0}(\hat{R}_{0,i}) = \hat{R}_{0,i}\mu_{\dot{R}}, \qquad \mu_{0,1}(\hat{R}_{0,i}) = \sqrt{\frac{p_0}{\rho_0}}\,\mu_{\dot{R}}, \\ \mu_{2,0}(\hat{R}_{0,i}) = \hat{R}_{0,i}^2\left(\mu_{\dot{R}}^2 + \sigma_{\dot{R}}^2\right), \qquad \mu_{1,1}(\hat{R}_{0,i}) = \hat{R}_{0,i}\sqrt{\frac{p_0}{\rho_0}}\left(\mu_{\dot{R}}\mu_{\dot{R}} + \rho_{R\dot{R}}\sigma_R\sigma_{\dot{R}}\right), \\ \mu_{0,2}(\hat{R}_{0,i}) = \frac{p_0}{\rho_0}\left(\mu_{\dot{R}}^2 + \sigma_{\dot{R}}^2\right)\end{gathered} \tag{20}$$

where $p_0$ and $\rho_0$ are the reference pressure and density at ambient conditions. The bubble radius abscissa $R_{j,i}$ is calculated using the CHyQMOM procedure (Fox et al., 2018) at all 4 quadrature nodes as

$$\overline{R}_{\pm,i} = \mu_{1,0,i} \pm \sqrt{\mu_{2,0,i} - \mu_{1,0,i}^2}, \qquad R_{1,i} = R_{2,i} = \overline{R}_{-,i}, \qquad R_{3,i} = R_{4,i} = \overline{R}_{+,i} \tag{21}$$

The conditional velocity abscissae $\dot{R}_{j,i}$ at the quadrature nodes are subsequently calculated as

$$\begin{gathered}\overline{\dot{R}}_{\pm,i} = \mu_{0,1,i} \pm \frac{\mu_{1,1,i} - \mu_{1,0,i}\mu_{0,1,i}}{\sqrt{\mu_{2,0,i} - \mu_{1,0,i}^2}}, \qquad s_i = \sqrt{\mu_{0,2,i} - \mu_{0,1,i}^2 - \frac{(\mu_{1,1,i} - \mu_{1,0,i}\mu_{0,1,i})^2}{\mu_{2,0,i} - \mu_{1,0,i}^2}}, \\ \dot{R}_{1,i} = \overline{\dot{R}}_{-,i} - s_i, \qquad \dot{R}_{2,i} = \overline{\dot{R}}_{-,i} + s_i, \qquad \dot{R}_{3,i} = \overline{\dot{R}}_{+,i} - s_i, \qquad \dot{R}_{4,i} = \overline{\dot{R}}_{+,i} + s_i\end{gathered} \tag{22}$$

The bubble radius $R_{j,i}$ is initialized at the 4 quadrature nodes for all $\hat{R}_{0,i}$ bins as

$$R_{1,i} = R_{2,i} = \hat{R}_{0,i}\left(\mu_R - \sigma_R\right), \qquad R_{3,i} = R_{4,i} = \hat{R}_{0,i}\left(\mu_R + \sigma_R\right) \tag{23}$$

Parameters $\mu_R$ and $\sigma_R$ are normalized using the equilibrium radius $\hat{R}_{0,i}$ at each bin. The bubble pressure $p_{b_{j,i}}$ and vapor mass $m_{v_{j,i}}$ are set at each quadrature node via an isothermal mapping (Preston et al., 2007),

$$m_{v_{j,i}} = m_{v_{0,i}}\frac{R_{j,i}^3}{\hat{R}_{0,i}^3}, \qquad p_{b_{j,i}} = p_{b_{0,i}}\frac{\hat{R}_{0,i}^3\left(m_{g_{0,i}} + m_{v_{j,i}}\right)}{R_{j,i}^3\left(m_{g_{0,i}} + m_{v_{0,i}}\right)} \tag{24}$$

where $m_{g_{0,i}}$ and $m_{v_{0,i}}$ are the mass of gas and vapor at the equilibrium radius $\hat{R}_{0,i}$ evaluated using the ideal gas law. All bubbles in a bin share the gas content that defines $\hat{R}_{0,i}$. For nonzero $\sigma_R$, the node radii differ from $\hat{R}_{0,i}$. With fixed gas content, these nodes are not in mechanical, thermal, and vapor-mass equilibrium at the ambient pressure. Thus, (24) maps the equilibrium gas–vapor state isothermally to each node radius. The gas mass and temperature are fixed, and the vapor mass scales with the bubble volume. The Monte Carlo samples use the same mapping, and Section 4 reports how the initial radius spread affects the closure error. This procedure assumes that $p_b$ and $m_v$ take one value at each $(R, \dot{R})$ node, so their conditional densities are delta functions. Each node thus carries one thermodynamic history, advanced via (25). Bubbles that reach the same $(R, \dot{R})$ via different histories share one value of $p_b$ and $m_v$. Section 4 measures the spread of $p_b$ at fixed $(R, \dot{R})$ in Monte Carlo samples. The bubble dynamic equations in (18) are evaluated at the quadrature nodes of each $\hat{R}_0$ bin as

$$\begin{aligned}\dot{m}_{v_{j,i}} &= \frac{4\pi R_{j,i}^2 D\rho_{bw}}{1 - \chi_{vw}}\frac{\partial \chi_{vw}}{\partial r}\bigg|_{r=R_{j,i}}, \\ \dot{p}_{b_{j,i}} &= \frac{3\gamma_b}{R_{j,i}}\left(-\frac{\partial R_{j,i}}{\partial t}p_{b_{j,i}} + R_v T_{bw}\frac{\dot{m}_{v_{j,i}}}{4\pi R_{j,i}^2} + \frac{\gamma_b - 1}{\gamma_b}k_{bw}\frac{\partial T}{\partial r}\bigg|_{r=R_{j,i}}\right)\end{aligned} \tag{25}$$

where $\partial R_{j,i}/\partial t$ is the rate of change of the radius abscissae at the four nodes, which differs from the velocity abscissae $\dot{R}_{j,i}$. We use $\partial R_{j,i}/\partial t$ to advance $p_b$ since $\partial R/\partial t = \dot{R}$ holds only for the ensemble mean. The PBE gives $\dot{\mu}_{10} = \mu_{01}$ and $\dot{\mu}_{20} = 2\mu_{11}$ for a spatially homogeneous population. By (26), $(\partial R_{1,i}/\partial t + \partial R_{3,i}/\partial t)/2 = \dot{\mu}_{10} = \mu_{01}$, so the first two radius moments of the reconstruction satisfy the PBE. Using $\partial R_j/\partial t$ in (25) adds no closure beyond the second-order quadrature of (14). Nodes with the same radius abscissa have the same $\partial R_j/\partial t$ and initial state (24), and the wall fluxes depend only on the node radius and thermodynamic state. Thus, nodes 1 and 2 share one value of $p_b$ and $m_v$, as do nodes 3 and 4. The velocity abscissae enter the ensemble pressure through the viscous and kinetic terms in (2) and (17). Differentiating the hyperbolic inversion of Fox et al. (2018) gives

$$\begin{aligned}\frac{\partial R_{1,i}}{\partial t} &= \frac{\partial R_{2,i}}{\partial t} = \frac{\partial \mu_{1,0,i}}{\partial t} - \frac{\dfrac{\partial \mu_{2,0,i}}{\partial t} - 2\mu_{1,0,i}\dfrac{\partial \mu_{1,0,i}}{\partial t}}{2\sqrt{\mu_{2,0,i} - \mu_{1,0,i}^2}}, \\ \frac{\partial R_{3,i}}{\partial t} &= \frac{\partial R_{4,i}}{\partial t} = \frac{\partial \mu_{1,0,i}}{\partial t} + \frac{\dfrac{\partial \mu_{2,0,i}}{\partial t} - 2\mu_{1,0,i}\dfrac{\partial \mu_{1,0,i}}{\partial t}}{2\sqrt{\mu_{2,0,i} - \mu_{1,0,i}^2}},\end{aligned} \tag{26}$$

The time derivatives of $\mu_{1,0,i}$ and $\mu_{2,0,i}$ follow from the conservative transport Eqs. (10) as

$$\frac{\partial \mu_{1,0,i}}{\partial t} = \frac{1}{n}\left(\frac{\partial\left(n\mu_{1,0,i}\right)}{\partial t} - \mu_{1,0,i}\frac{\partial n}{\partial t}\right), \qquad \frac{\partial \mu_{2,0,i}}{\partial t} = \frac{1}{n}\left(\frac{\partial\left(n\mu_{2,0,i}\right)}{\partial t} - \mu_{2,0,i}\frac{\partial n}{\partial t}\right) \tag{27}$$

where $\partial(n\mu_{1,0,i})/\partial t$ and $\partial(n\mu_{2,0,i})/\partial t$ are calculated using (10). Since $\mu_{0,0,i} = 1$, $\partial n/\partial t$ in (27) follows from

$$\frac{\partial n}{\partial t} + \nabla\cdot(n\boldsymbol{u}) = 0, \tag{28}$$

recovering the number-density conservation law (4). When $\mu_{2,0,i} - \mu_{1,0,i}^2 < 0$, the moments are not realizable. The implementation floors the radius variance in the univariate inversion,

$$\mu_{2,0,i} - \mu_{1,0,i}^2 \leftarrow \max\left(\mu_{2,0,i} - \mu_{1,0,i}^2,\ \sigma_\epsilon\right), \tag{29}$$

where $\sigma_\epsilon = 10^{-16}$. The conditional velocity variance under the square root in $s_i$ is also floored at $\sigma_\epsilon$. The floor acts only inside the square roots of the inversion. It can shift the abscissae near the realizability boundary, though the transported moments are unchanged. The floor is not activated in the zero-dimensional calculations of Section 4, and Section 5 reports its activation frequency for a representative bubble screen.

## 3. Numerical method

An interface-capturing finite-volume scheme evolves the governing equations for the liquid and dispersed phases. The conservative variables $\vec{q}_c$ are evolved in the cell centers according to

$$\frac{\partial \vec{q}_c}{\partial t} + \nabla\cdot\vec{F} = \vec{s} \tag{30}$$

The source vector $\vec{s}$ includes the moment sources $n\vec{g}$ of (10) and the void-fraction growth/collapse source on the right-hand side of (6). In MFC, $p_{b_{j,i}}$ and $m_{v_{j,i}}$ are stored in separate node arrays outside $\vec{q}_c$ and are not advected. Their right-hand sides (25) are evaluated at every SSP–RK stage and advanced with the same coefficients and time step as the conservative state. Advection of the moments enters the $p_b$ update through $\partial R_{j,i}/\partial t$, computed via (26), (27), and (28). The conservative variables $\vec{q}_c$ are converted to their primitive forms $\vec{q}_p$. The primitive variables are then reconstructed at the cell boundaries using a fifth-order WENO scheme (Jiang and Shu, 1996). The fluxes $\vec{F}$ are computed using an HLLC approximate Riemann solver (Toro et al., 1994). A third-order strong-stability-preserving Runge–Kutta (SSP–RK) scheme

**Table 1**
Ranges of the dimensionless groups of (19) over all saved times and quadrature nodes in the zero-dimensional verification case. The thermal and mass Fourier numbers use one forcing period, $\tau_d = 2t_0$.

| Diagnostic | Minimum | Maximum |
|---|---|---|
| $\mathrm{Re}_R$ | $1.53 \times 10^{-2}$ | 52.7 |
| $\mathrm{We}_R$ | $3.25 \times 10^{-7}$ | 4.03 |
| $\mathrm{Pe}_T$ | $5.98 \times 10^{-4}$ | 2.07 |
| $\mathrm{Pe}_m$ | $6.32 \times 10^{-4}$ | 2.18 |
| $\mathrm{Fo}_T$ | 0.317 | 0.801 |
| $\mathrm{Fo}_m$ | 0.300 | 0.759 |

advances the conservative variables. Section 5 examines the sensitivity to the equilibrium-radius discretization, spatial grid, and time step.

## 4. Model verification

We first verify the model for a monodisperse population of air bubbles in water. The liquid pressure $p_l$ is explicitly set to $p_l = p_0(1 + A\sin(\omega t))$ where $p_0$ is the reference pressure and $t$ is the simulation time. This configuration does not solve (1), and only (10) and the node values of $p_b$ and $m_v$ are advanced. For our simulation, we set $A = 0.5$ and $\omega = \pi$. This corresponds to an excitation frequency that is 1.53 times the Minnaert frequency. We non-dimensionalize lengths by the reference equilibrium radius $R_{0,\mathrm{ref}} = 10\,\mu\mathrm{m}$. The bubble population is initialized with means $\mu_R = R_0 = 1$ and $\mu_{\dot R} = 0$, standard deviations $\sigma_R = \sigma_{\dot R} = 0.1$, and $\rho_{R\dot R} = 0$.

The reference pressure and density of the liquid are set as $p_0 = 101\,325\,\mathrm{Pa}$ and $\rho_0 = 1000\,\mathrm{kg/m^3}$. The gas specific heat ratio is $\gamma_b = 1.4$, and the liquid speed of sound is $c_l = 1475\,\mathrm{m/s}$. Surface tension, viscosity, and vapor pressure of the liquid are set at $\sigma_l = 0.072\,75\,\mathrm{N/m}$, $\mu_l = 1.002 \times 10^{-3}\,\mathrm{Pa\,s}$, and $p_v = 2338.8\,\mathrm{Pa}$. The thermodynamic parameters associated with the constant-transfer model are calculated using a water vapor and air mixture, with the thermodynamic properties and bubble wall closures defined by Preston et al. (2007). The bubble dynamics is simplified to use the Rayleigh–Plesset equation, which is the incompressible version of (16). The time step $\Delta t$ is set to $0.0005\,t_0$, where $t_0 = R_{0,\mathrm{ref}}\sqrt{\rho_0/p_0}$ is the reference time.

We evaluate the dimensionless groups of (19) at every saved time and quadrature node. The dimensional node states use $R_{0,\mathrm{ref}} = 10^{-5}\,\mathrm{m}$, $p_0 = 101325\,\mathrm{Pa}$, and $\rho_0 = 1000\,\mathrm{kg\,m^{-3}}$. The transport properties are constant, with $a_g = k_g/(\rho_g c_{p,g}) = 2.556 \times 10^{-5}\,\mathrm{m^2\,s^{-1}}$ and $D = 2.42 \times 10^{-5}\,\mathrm{m^2\,s^{-1}}$. The dynamic time scale is one forcing period, $\tau_d = 2t_0$, since the nondimensional forcing frequency is $\omega = \pi$. Table 1 lists the resulting ranges.

The minima of $\mathrm{Re}_R$, $\mathrm{We}_R$, and the Péclet numbers occur where $\dot R$ changes sign. The Péclet numbers range from diffusion-dominated values to order unity over each oscillation. The Fourier numbers are of order unity, so thermal and species diffusion act over each forcing period. The maximum radial Weber number is 4.03, so surface tension is not negligible at the fastest nodes.

We compare with Monte Carlo simulations sampled from a multivariate Gaussian distribution for $R$ and $\dot R$ with the same means and standard deviations. We sample $N_s = 1000$ bubbles, integrate each one, and use their average as a surrogate for the true solution. Charalampopoulos et al. (2022) found $N_s = 1000$ sufficient for similar Monte Carlo calculations with a polytropic closure. The RMS error $\|e\|_2$ for a particular bubble variable $v$ is calculated using

$$\|e\|_2 = \frac{1}{\sqrt{N_t}}\sqrt{\sum_{i=0}^{N_t-1}\left(\frac{v^{(\mathrm{QBMM})}(t_i) - v^{(\mathrm{MC})}(t_i)}{v^{(\mathrm{MC})}(t_i)}\right)^2} \tag{31}$$

where $v$ is $R$, $p_b$, $m_v$, or a moment $\mu_{lm}$. Table 2 compares $\|e\|_2$ of $R$, $p_b$, and $m_v$ for the constant-transfer model with that of the polytropic model (Bryngelson et al., 2023). The polytropic model does not advance $p_b$ or $m_v$, so these entries are marked ✗. The mean-radius error of the constant-transfer model is 1.4× that of the polytropic model. A pseudo-polytropic case isolates the effect of advancing $p_b$ at the nodes. It sets $k_{bw} = 0$ and uses the infinite-rate mass-transfer limit, for which the ODE for $p_b$ in (18) becomes

$$\dot p_b = -\frac{3\gamma_b}{R}\dot R\left(p_b - p_v\right) \tag{32}$$

where $p_v$ is the vapor pressure. Thus, $p_b$ follows a polytropic relation at each node, and the initial condition is exact. This pseudo-polytropic case is analytically equivalent to the polytropic closure. Both cases give $\|e\|_2 = 0.58\,\%$ for $R$, identical to round-off. Thus, advancing $p_b$ at the nodes does not increase the radius error when an exact polytropic mapping exists.

**Table 2**
RMS relative error $\|e\|_2$ of the QBMM closures with respect to Monte Carlo simulations with $N_s = 1000$.

| $10^2\,\|e\|_2$ | Polytropic | Constant transfer | Pseudo polytropic |
|---|---|---|---|
| $R$ | 0.58 | 0.81 | 0.58 |
| $p_b$ | ✗ | 2.62 | ✗ |
| $m_v$ | ✗ | 3.49 | ✗ |

**Table 3**
RMS relative error $10^2\,\|e\|_2$ between QBMM and Monte Carlo ($N_s = 1000$) for varying initial radius spread $\sigma_R$ and fixed $\sigma_{\dot R} = 0.1$.

| | $R$ | | $p_b$ | $m_v$ | $\overline{R^3 p_{bw}}$ |
|---|---|---|---|---|---|
| $\sigma_R$ | Polytropic | Constant transfer | Constant transfer | | |
| 0.05 | 0.28 | 0.39 | 1.31 | 1.74 | 0.30 |
| 0.1 | 0.58 | 0.81 | 2.62 | 3.49 | 0.60 |
| 0.2 | 1.64 | 1.76 | 6.59 | 7.05 | 1.40 |

Table 3 repeats the comparison for $\sigma_R = 0.05$ and 0.2, with the Monte Carlo samples drawn from the same random numbers. The errors of both closures increase with $\sigma_R$, which sets how far the initial population is from equilibrium. Over this range, the constant-transfer mean-radius error exceeds the polytropic error by 0.1 to 0.2 percentage points. These calculations do not separate the contributions of the isothermal initialization and the node closure to this excess. Fig. 2 compares the mean radius and mean bubble pressure of the constant-transfer model with the Monte Carlo results. Fig. 3 shows that the quadrature nodes follow the Monte Carlo probability density at four times.

**Table 4**
Constant-transfer QBMM and Monte Carlo ($N_s = 1000$) results for increasing forcing amplitude $A$, where $\gamma_R$ and $b_R$ are the sample skewness and bimodality coefficient of $R$, and maxima are over all saved times.

| | $A = 0.5$ | $A = 0.75$ | $A = 1$ |
|---|---|---|---|
| $\min_t \overline{R}$ | 0.88 | 0.82 | 0.76 |
| $\max_t \lvert\gamma_R\rvert$ | 0.92 | 1.56 | 3.59 |
| $\max_t b_R$ | 0.42 | 0.48 | 0.53 |
| $10^2\,\|e\|_2$ for $R$ | 0.81 | 1.09 | 1.56 |
| $10^2\,\|e\|_2$ for $p_b$ | 2.62 | 4.07 | 6.18 |
| $10^2\,\|e\|_2$ for $m_v$ | 3.49 | 4.82 | 7.11 |
| $10^2\,\|e\|_2$ for $\overline{R^3 p_{bw}}$ | 0.60 | 0.93 | 1.40 |

The delta-function closure assumes that $p_b$ and $m_v$ are determined by the node state, and the Monte Carlo samples test this assumption. At each saved time, a least-squares fit of the sample bubble pressures that is cubic in $R$ and quadratic in $\dot R$ accounts for at least 99.9 % of their variance. A cubic fit in $R$ alone accounts for a median of 98.4 %, with a residual standard deviation of at most 4.7 % of the mean bubble pressure. The node pressures agree with this conditional mean, evaluated at the radius abscissae, to within 2.3 % in RMS relative difference. The closed term $\overline{R^3 p_{bw}}$ that enters (2) has an RMS relative error of 0.60 %, smaller than the 2.62 % error in the mean bubble pressure.

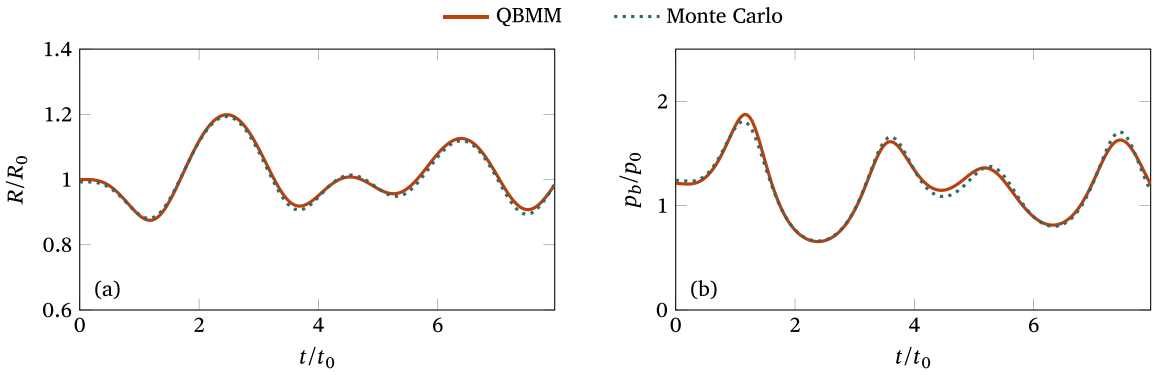



**Fig. 2.** Comparison of the evolution of (a) the mean bubble radius and (b) the mean bubble pressure, for the constant-transfer QBMM and Monte Carlo simulations of a monodisperse bubble population.

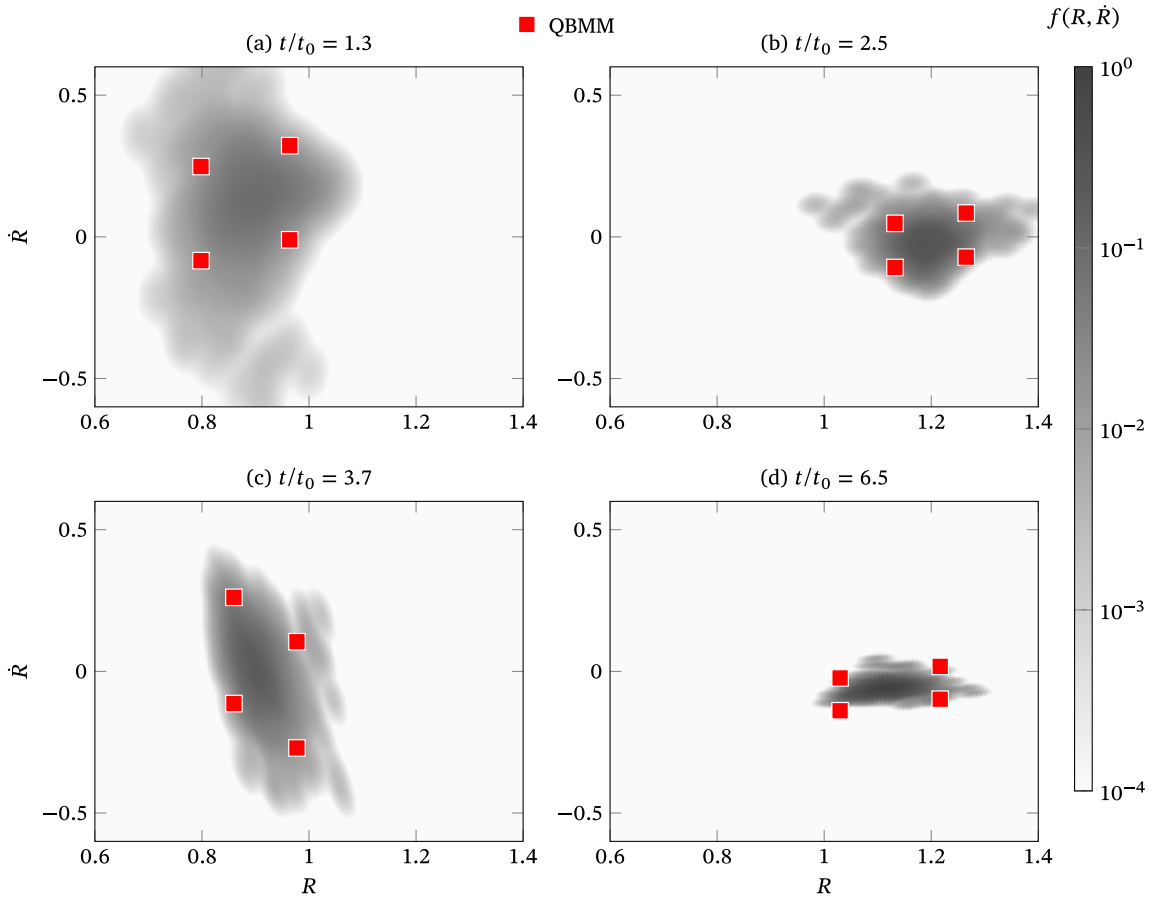



**Fig. 3.** Evolution of the probability density $f(R,\dot{R})$ from Monte Carlo simulation ($N_s = 1000$) and the four equal-weight ($\hat{w}_j = 1/4$) quadrature nodes of the constant-transfer QBMM at four times.

We repeat the verification with forcing amplitudes $A = 0.75$ and 1. For $A = 1$, the liquid pressure vanishes once per forcing period. As $A$ increases from 0.5 to 1, the minimum mean radius decreases from 0.88 to 0.76 and the sample skewness of $R$ increases from 0.92 to 3.59 (Table 4). The bimodality coefficient (Pfister et al., 2013) reaches 0.53 for $A = 1$, below the bimodality threshold of 5/9. The relative errors increase by a factor of 1.9 to 2.4 between $A = 0.5$ and $A = 1$, though the error in $\overline{R^3 p_{bw}}$ remains at or below 1.4 %. Thus, the four-node closure loses accuracy as the distribution becomes more skewed.

## 5. Application to bubble screens

We test the model on an acoustically excited, dilute, polydisperse 1D bubble screen. The bubble screen is initialized with a void fraction of

$\alpha_b = 4 \times 10^{-5}$ and a log-normal PDF with mean radius $R_0 = 1$, non-dimensionalized by the reference bubble radius $R_{0,\mathrm{ref}} = 10\,\mu\mathrm{m}$. This void fraction is in the dilute regime of the ensemble-averaged model. Direct bubble–bubble interactions, coalescence, breakup, boundary-layer overlap, and deformation are neglected, and the bubbles interact only through the mixture pressure. The bubble screen length is set to $L_b = 400R_0$ and is centered in a 1D domain of length $5L_b$, with $N_x = 1600$ grid points. The thermodynamic parameters are those of Section 4. A one-way sinusoidal pressure pulse with peak amplitude $10^5$ Pa ($0.99p_0$) excites the bubble screen. The pulse frequency is 300 kHz, 0.91 times the Minnaert frequency of 328 kHz for an adiabatic gas ($\gamma_b = 1.4$) with negligible surface tension and viscosity. Neumann boundary conditions are used along the pulse direction. The acoustic source is located $250R_0$ from the center of the bubble screen with a support width spanning 15 grid spacings. The bubble population is polydisperse, with $n_b = \{9, 21, 31, 51\}$ bins. Closure errors are measured with respect to a reference solution with $n_b = 91$. Across all parameter combinations plotted in Figs. 4–6, including log-normal widths $\sigma_{R_0} =$ 0.1–0.3, the largest $n_b = 51$ RMS relative error with respect to $n_b = 91$ is 0.026 %. Thus, $n_b = 51$ is converged for these log-normal distributions. Bryngelson et al. (2019) found similar bin counts sufficient for the method of classes. The standard deviation of the log-normal PDF is varied as $\sigma_{R_0} = \{0.1, 0.2, 0.3\}$. The initial distribution for the moment set is a joint Gaussian distribution with means $\mu_R = 1$ and $\mu_{\dot{R}} = 0$, with the standard deviations varied as $\sigma_R = \{0.1, 0.2, 0.3\}$ and $\sigma_{\dot{R}} = \{0.1, 0.2, 0.3\}$. For each variation, we report the pressure $p$ at the center of the bubble screen and its closure error as a function of $n_b$. The pressure is non-dimensionalized by the reference pressure $p_0$ and the time by $t_0 = R_{0,\mathrm{ref}}\sqrt{\rho_0/p_0}$. The bubble dynamics follow the Keller–Miksis Eq. (16). We then compare with the polytropic model of Bryngelson et al. (2023). Finally, we compare a 3D bubble screen with a volume-averaged Euler–Lagrange model (Vaca-Revelo et al., 2026). The CFL number is 0.1 for the 1D calculations and 0.2 for the 3D Euler–Euler and Euler–Lagrange calculations. The Keller–Miksis equation assumes spherical bubbles. The radial Weber number $\mathrm{We}_R$ indicates where shape modes may matter. Table 5 lists the ranges of the groups in (19) for the representative case, $(\sigma_R, \sigma_{\dot{R}}, \sigma_{R_0}) = (0.2, 0.2, 0.3)$ and $n_b = 51$, over the four nodes, 51 bins, 321 grid points in the screen, and 201 saved times. The Fourier numbers use one forcing period, $\tau_d = (300\,\mathrm{kHz})^{-1} \simeq 3.36t_0$.

As in Table 1, the minima occur where $\dot{R}$ changes sign. The Péclet numbers reach about 10, and the Fourier numbers range from $2.4\times10^{-2}$ to 29.6. The maximum radial Weber number is 57.0, so surface tension is weak compared to inertia at the largest radial speeds, and the bubbles may deform there. For the representative case with $\sigma_\epsilon = 10^{-16}$, the variance floor (29) is activated 27 times across 1600 grid cells and 24,000 time steps. With $\sigma_\epsilon = 10^{-14}$ and $10^{-18}$, the center-pressure history does not change visibly. We repeat the representative case with $n_b = 181$. The maximum relative difference between the $n_b = 91$ and $n_b = 181$ center-pressure histories is $7.4\times10^{-4}$%, and the $n_b = 51$ error is 0.0156% with respect to either. Thus, $n_b = 91$ is a converged reference. We also repeat this case with $N_x = 800$ and 3200 grid cells. The maximum relative difference in the center pressure is 4.2% between $N_x = 800$ and 1600 and 1.4% between $N_x = 1600$ and 3200, and the $N_x = 800$ solution differs from the $N_x = 3200$ solution by 5.6%. We use $N_x = 1600$. For $N_x = 1600$ and CFL numbers of 0.2 and 0.3, the maximum relative difference from the CFL = 0.1 center pressure is 0.185% and 0.197%, respectively. Thus, the results are insensitive to the time step for CFL $\leq 0.3$.

### 5.1. Varying $\sigma_R$

We first fix $\sigma_{\dot{R}} = 0.2$ and $\sigma_{R_0} = 0.3$ and vary $\sigma_R = \{0.1, 0.2, 0.3\}$. Fig. 4(b) shows the closure error as a function of $n_b$. The error $\|e\|_2$ increases slightly with $\sigma_R$, in contrast to the polytropic results of Bryngelson et al. (2023). At $n_b = 51$, the center pressure lacks the high-frequency components at the bubble natural frequency that appear in Bryngelson et al. (2023). The minimum radius during collapse decreases slightly as $\sigma_R$ increases.

**Table 5**
Ranges of the dimensionless groups of (19) over all active quadrature-node evaluations in the representative one-dimensional bubble-screen case with $n_b = 51$. The thermal and mass Fourier numbers use one forcing period, $\tau_d \simeq 3.36t_0$.

| Diagnostic | Minimum | Maximum |
|---|---|---|
| $\mathrm{Re}_R$ | $1.21\times10^{-7}$ | 263 |
| $\mathrm{We}_R$ | $5.76\times10^{-17}$ | 57.0 |
| $\mathrm{Pe}_T$ | $4.71\times10^{-9}$ | 10.4 |
| $\mathrm{Pe}_m$ | $4.97\times10^{-9}$ | 10.9 |
| $\mathrm{Fo}_T$ | $2.56\times10^{-2}$ | 29.6 |
| $\mathrm{Fo}_m$ | $2.42\times10^{-2}$ | 28.1 |

### 5.2. Varying $\sigma_{\dot{R}}$

Next, we fix $\sigma_R = 0.2$ and $\sigma_{R_0} = 0.3$ and vary $\sigma_{\dot{R}} = \{0.1, 0.2, 0.3\}$. Fig. 5(b) shows that $\|e\|_2$ does not change with $\sigma_{\dot{R}}$, as for the polytropic model (Bryngelson et al., 2023). The center pressure at $n_b = 51$ is also insensitive to $\sigma_{\dot{R}}$. Thus, the center pressure and its error are more sensitive to $\sigma_R$ than to $\sigma_{\dot{R}}$.

### 5.3. Varying $\sigma_{R_0}$

Finally, we fix $\sigma_R = \sigma_{\dot{R}} = 0.2$ and vary the width of the log-normal PDF, $\sigma_{R_0} = \{0.1, 0.2, 0.3\}$. Fig. 6(b) shows that $\|e\|_2$ increases with $\sigma_{R_0}$. This is because a broader distribution has a larger truncation error in Simpson's rule. The center pressure oscillates longer as $\sigma_{R_0}$ decreases. The high-frequency oscillations of Bryngelson et al. (2023) at larger $\sigma_{R_0}$ are absent with the constant-transfer model.

### 5.4. Comparison to polytropic model

Fig. 7 compares the center pressure of the constant-transfer and polytropic models for $\sigma_R = \sigma_{\dot{R}} = 0.2$, $\sigma_{R_0} = 0.3$, and $n_b = 51$. Both models respond similarly to the long-wavelength input. However, the constant-transfer model attenuates the short-wavelength oscillations at the natural frequencies of the bubble screen. The difference is largest for $t/t_0 > 20$, after the wave has passed and the pressure has equilibrated. After removing the mean, the RMS pressure fluctuation over $20 \leq t/t_0 \leq 30$ is $1.15\times10^{-2}p_0$ for the polytropic closure and $1.21\times10^{-3}p_0$ for constant transfer. The corresponding peak-to-peak values are $4.61\times10^{-2}p_0$ and $4.37\times10^{-3}p_0$. The dominant nonzero Fourier component of the polytropic record occurs at $ft_0 \simeq 0.399$, where its amplitude is $9.57\times10^{-3}p_0$, compared with $4.99\times10^{-4}p_0$ for constant transfer. The two calculations share the same moment set, quadrature, and numerical discretization, so this difference is due to the bubble-pressure closure. Heat transfer at the bubble wall damps micrometer-sized bubbles driven near resonance (Plesset and Prosperetti, 1977; Commander and Prosperetti, 1989). The constant-transfer closure includes this thermal damping. The adiabatic polytropic closure has only viscous and acoustic-radiation damping.

### 5.5. Comparison to Euler–Lagrange model

We compare the constant-transfer model with the Euler–Lagrange model of Vaca-Revelo et al. (2026). Each Lagrangian bubble follows the Keller–Miksis equation with the same reduced-order heat and mass transfer at the bubble wall, so this comparison tests the quadrature and node closure of the Euler–Euler model. The bubble screen length for this calculation is $L_b = 500R_0$, with the domain length $L_x = 8L_b$. The bubble screen is extended to 3D with $L_y = L_z = L_b$ and

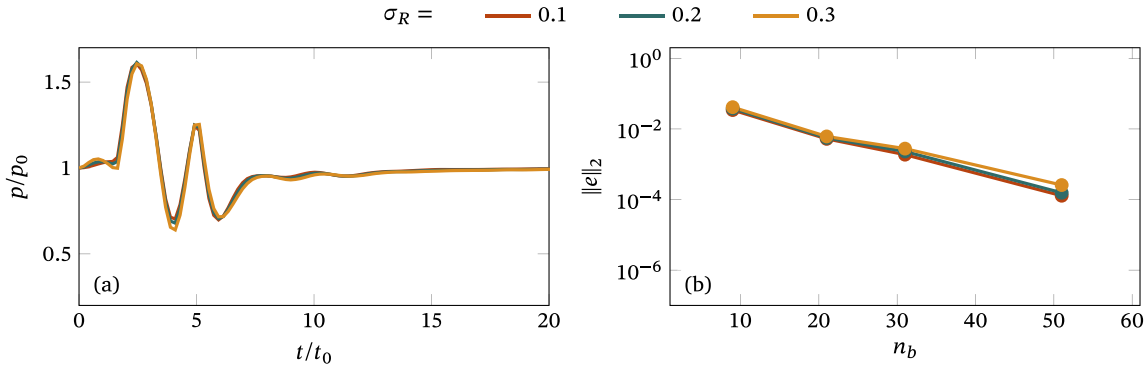



**Fig. 4.** (a) Dimensionless pressure $p/p_0$ versus time $t/t_0$ at the center of the bubble screen at $n_b = 51$. (b) RMS relative error $\|e\|_2$ for the pressure for a varying number of bins $n_b$, with a reference solution at $n_b = 91$. Both are shown at varying values of $\sigma_R$ and fixed $\sigma_{\dot{R}} = 0.2$ and $\sigma_{R_0} = 0.3$.

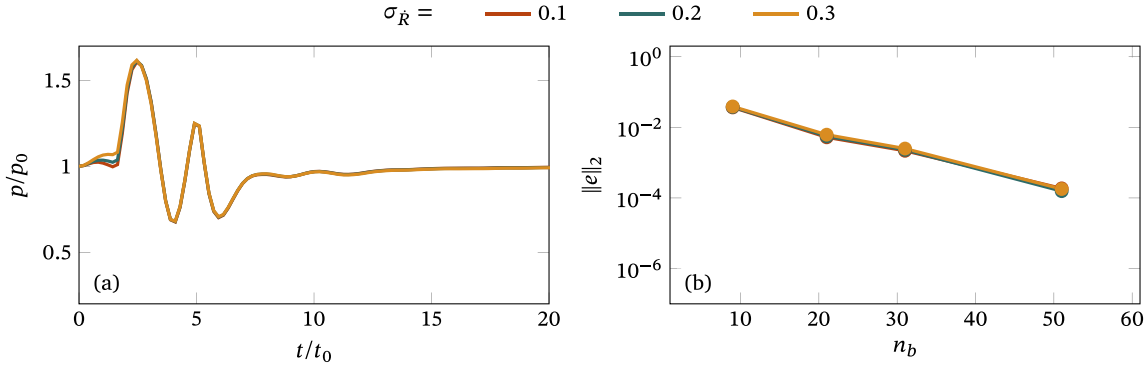



**Fig. 5.** (a) Dimensionless pressure $p/p_0$ versus time $t/t_0$ at the center of the bubble screen at $n_b = 51$. (b) RMS relative error $\|e\|_2$ for the pressure for a varying number of bins $n_b$, with a reference solution at $n_b = 91$. Both are shown at varying values of $\sigma_{\dot{R}}$ and fixed $\sigma_R = 0.2$ and $\sigma_{R_0} = 0.3$.

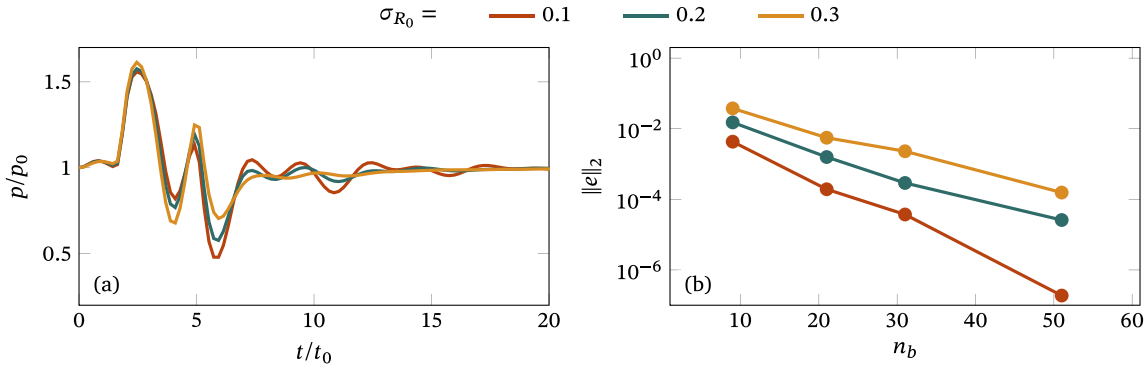



**Fig. 6.** (a) Dimensionless pressure $p/p_0$ versus time $t/t_0$ at the center of the bubble screen at $n_b = 51$. (b) RMS relative error $\|e\|_2$ for the pressure for a varying number of bins $n_b$, with a reference solution at $n_b = 91$. Both are shown at varying values of $\sigma_{R_0}$ and fixed $\sigma_R = \sigma_{\dot{R}} = 0.2$.

periodic boundary conditions in the transverse directions. The grid resolution is coarsened to $(N_x, N_y, N_z) = 400\times50\times50$. The grid spacing exceeds the maximum Lagrangian bubble radius and still resolves the sinusoidal input. The Lagrangian bubbles are placed uniformly within the bubble screen of width $L_b$. We set $\sigma_{R_0} = 0.3$ and sample the radii of the Lagrangian bubbles from the log-normal PDF to satisfy $\alpha_b = 4 \times 10^{-5}$ within the bubble screen. Following Bryngelson et al. (2019), Vaca-Revelo et al. (2026), we average $N_{\text{sim}} = 40$ independent Euler–Lagrange simulations to reduce sampling error. The Euler–Euler simulation uses $\sigma_R = \sigma_{\dot{R}} = 0.2$ and $n_b = 51$. Fig. 8 compares the center pressure of the two models, which differ by an RMS relative error of 1.5 %. During the early driven and collapse phases, the Euler–Euler curve leaves the minimum–maximum envelope of the Euler–Lagrange results by up to about 4 % of $p_0$. This discrepancy occurs during the fastest transient, when each Euler–Lagrange realization contains a finite random bubble population that is then volume averaged. Thus, the envelope measures the spread of 40 realizations. The two models also agree in the frequency domain. After removing the mean, over $10 \le t/t_0 \le 25$ (frequency resolution $\Delta f\, t_0 \simeq 0.067$), the RMS pressure fluctuation is $2.46\times10^{-2}p_0$ for the constant-transfer Euler–Euler model and $2.51\times10^{-2}p_0$ for the Euler–Lagrange mean. Both records have the same dominant component, $f t_0 \simeq 0.200$, with amplitudes $2.25\times10^{-2}p_0$ and $2.26\times10^{-2}p_0$, respectively. At this frequency, the Euler–Euler phase

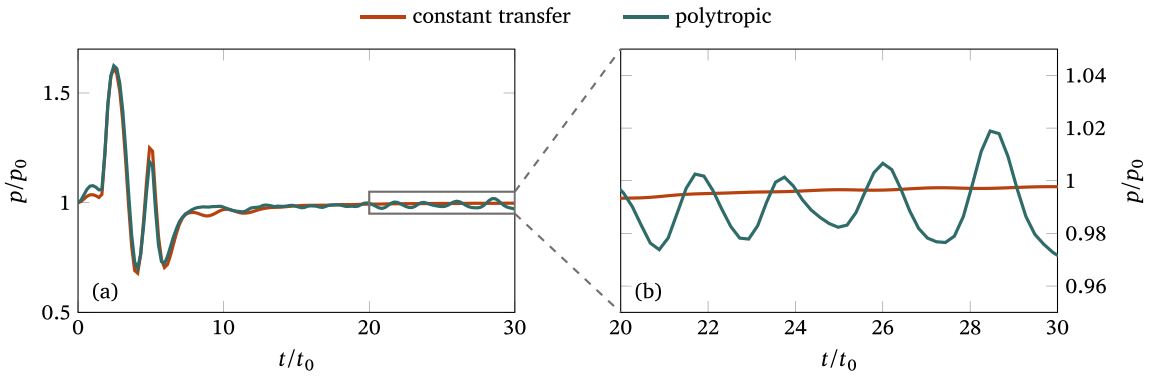



**Fig. 7.** (a) Dimensionless pressure $p/p_0$ versus time $t/t_0$ at the center of the bubble screen for the constant-transfer model and the polytropic model at $\sigma_R = \sigma_{\dot{R}} = 0.2$, $\sigma_{R_0} = 0.3$, and $n_b = 51$. (b) Detail of the outlined window $20 \le t/t_0 \le 30$ of (a), after the pressure has equilibrated.

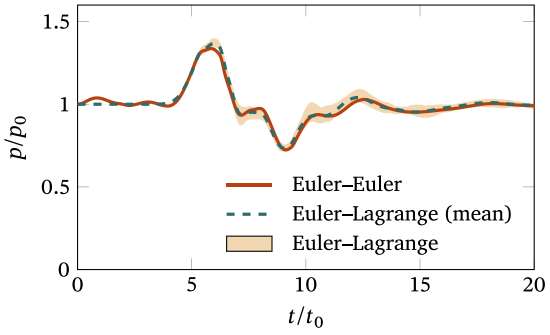



**Fig. 8.** Comparison of the dimensionless pressure $p/p_0$ at the center of the 3D bubble screen for the constant-transfer Euler–Euler model and the mean of 40 independent volume-averaged Euler–Lagrange simulations, with $\sigma_R = \sigma_{\dot{R}} = 0.2$, $\sigma_{R_0} = 0.3$, and $n_b = 51$. The band shows the minimum and maximum over the Euler–Lagrange simulations.

lags the Euler–Lagrange mean by 0.28 rad (4.4% of a period), and the correlation coefficient of the two fluctuation records is 0.94.

### 5.6. Computational cost and limitations

For each equilibrium-radius bin, both the previous polytropic formulation and the present method transport the same six moments, $(\mu_{00}, \mu_{10}, \mu_{01}, \mu_{20}, \mu_{11}, \mu_{02})$. The constant-transfer closure also stores $p_b$ and $m_v$ at four nodes, eight scalars per bin, with no finite-volume fluxes. Thus, the bubble state grows from six to fourteen scalars per cell and $R_0$ bin, a factor of 2.33. Storage and node-ODE cost remain linear in $n_b$. For the representative 3D bubble-screen problem in Section 5 with $n_b = 51$, the constant-transfer model uses about 10% more wall time and 21% more device memory than the polytropic model. The wall-time increase is small because most of the simulation time is spent in the conditional inversion and the reconstruction of the conservative variables. The cost of an Euler–Lagrange model instead scales with the number of sampled bubbles.

As in the previous polytropic implementation, large pressure ratios acting on small equilibrium radii can drive the radius toward zero and produce non-realizable moments. The variance floor in (29) does not prevent this failure.

## 6. Conclusion

We present an Euler–Euler sub-grid-scale model for polydisperse bubbly flows with heat and mass transfer. A population balance equation governs the distribution of bubble radius and radial velocity. A conditional hyperbolic inversion gives the quadrature nodes that close the moment transport equations and the ensemble-averaged terms. The constant-transfer closure adds the bubble-wall heat and vapor-mass transfer that the polytropic model omits. Bubble pressure and vapor mass are advanced at the quadrature nodes, so the PBE needs no additional internal variables and the transport keeps six moments per $R_0$ bin. The model is implemented in the compressible flow solver MFC. For a monodisperse population, the mean radius agrees with Monte Carlo simulations to within 0.81 %. In this verification case, the closure error roughly doubles as the forcing amplitude increases from $0.5p_0$ to $p_0$, and the error in $\overline{R^3 p_{bw}}$ stays at or below 1.4 %.

For an acoustically excited, polydisperse bubble screen, the constant-transfer model gives a late-time RMS pressure fluctuation of $1.21 \times 10^{-3} p_0$, compared with $1.15 \times 10^{-2} p_0$ for the polytropic model. With $n_b = 51$, the error relative to $n_b = 91$ is below 0.026 % for all distributions tested and increases with $\sigma_{R_0}$. The Euler–Euler pressure at the center of a 3D bubble screen agrees with the mean of 40 volume-averaged Euler–Lagrange simulations to within an RMS relative error of 1.5 %, and their dominant oscillations share one frequency, with amplitudes within 0.4 % and a phase lag of 0.28 rad.

The calculations here consider dilute ($\alpha_b = 4 \times 10^{-5}$), spherical bubble populations under acoustic forcing, with approximately unimodal initial distributions. The reduced-order wall model does not resolve liquid thermal fields or interactions between neighboring boundary layers. Dense clouds, nonspherical bubbles, and multimodal populations require extensions of this formulation. As for the polytropic implementation, large pressure ratios acting on small equilibrium radii produce non-realizable moments. For example, a strong shock passing over an immersed boundary produces non-realizable moments. Limiters for non-realizable moments and adaptive sub-stepping of the dispersed phase may remove this failure. Radius distributions with long tails during collapse, or with several modes, require higher-order conditional moments and a model for the spread of $p_b$ and $m_v$ at each node.

## CRediT authorship contribution statement

**Anand Radhakrishnan:** Writing – original draft, Visualization, Validation, Software, Methodology, Investigation, Formal analysis, Data curation, Conceptualization. **Spencer H. Bryngelson:** Writing – review & editing, Supervision, Resources, Methodology, Funding acquisition, Conceptualization.

## Declaration of competing interest

The authors declare that they have no known competing financial interests or personal relationships that could have appeared to influence the work reported in this paper.

## Acknowledgments

SHB acknowledges support from the US Office of Naval Research under grant number N00014-22-1-2519. This research used resources of the Oak Ridge Leadership Computing Facility at the Oak Ridge National Laboratory, which is supported by the Office of Science of the U.S. Department of Energy under Contract No. DE-AC05-00OR22725 (allocation CFD154, PI Bryngelson). This work also used PSC Bridges2 and NCSA Delta and Delta AI through allocation PHY210084 (PI Bryngelson) from the Advanced Cyberinfrastructure Coordination Ecosystem: Services & Support (ACCESS) program, which is supported by National Science Foundation grants #2138259, #2138286, #2138307, #2137603, and #2138296.

## Data availability

All results were produced using MFC, which is publically available under the MIT license at github.com/MFlowCode/MFC. The datasets generated during this study include simulation input files, example cases, random seeds, and the source code used to produce the reported results. These materials have been archived on Zenodo (version 1.0.0) and are publicly available at 10.5281/zenodo.21590440, corresponding to Git commit `c7d8fe135746`.

## References

Ando, K., Colonius, T., Brennen, C.E., 2011. Numerical simulation of shock propagation in a polydisperse bubbly liquid. Int. J. Multiph. Flow 37, 596–608.

Bryngelson, S.H., Colonius, T., Fox, R.O., 2020. QBMMlib: A library of quadrature-based moment methods. SoftwareX 12, 100615.

Bryngelson, S.H., Fox, R.O., Colonius, T., 2023. Conditional moment methods for polydisperse cavitating flows. J. Comput. Phys. 477, 111917.

Bryngelson, S.H., Schmidmayer, K., Colonius, T., 2019. A quantitative comparison of phase-averaged models for bubbly, cavitating flows. Int. J. Multiph. Flow 115, 137–143.

Bryngelson, S.H., Schmidmayer, K., Coralic, V., Meng, J.C., Maeda, K., Colonius, T., 2021. MFC: An open-source high-order multi-component, multi-phase, and multi-scale compressible flow solver. Comp. Phys. Comm. 266, 107396.

Buffo, A., Vanni, M., Marchisio, D.L., Fox, R.O., 2013. Multivariate quadrature-based moments methods for turbulent polydisperse gas–liquid systems. Int. J. Multiph. Flow 50, 41–57.

Charalampopoulos, A., Bryngelson, S.H., Colonius, T., Sapsis, T.P., 2022. Hybrid quadrature moment method for accurate and stable representation of non-Gaussian processes applied to bubble dynamics. Phil. Trans. R. Soc. A 380, 20210209.

Colonius, T., Hagmeijer, R., Ando, K., Brennen, C.E., 2008. Statistical equilibrium of bubble oscillations in dilute bubbly flows. Phys. Fluids 20, 040902.

Commander, K.W., Prosperetti, A., 1989. Linear pressure waves in bubbly liquids: Comparison between theory and experiments. J. Acoust. Soc. Am. 85, 732–746.

Fox, R.O., 2008. A quadrature-based third-order moment method for dilute gas–particle flows. J. Comput. Phys. 227, 6313–6350.

Fox, R.O., Laurent, F., Vié, A., 2018. Conditional hyperbolic quadrature method of moments for kinetic equations. J. Comput. Phys. 365, 269–293.

Heylmun, J.C., Kong, B., Passalacqua, A., Fox, R.O., 2019. A quadrature-based moment method for polydisperse bubbly flows. Comp. Phys. Comm. 244, 187–204.

Jiang, G.-S., Shu, C.-W., 1996. Efficient implementation of weighted ENO schemes. J. Comput. Phys. 126, 202–228.

Maeda, K., Colonius, T., 2018. Eulerian–Lagrangian method for simulation of cloud cavitation. J. Comput. Phys. 371, 994–1017.

McGraw, R., 1997. Description of aerosol dynamics by the quadrature method of moments. Aerosol Sci. Technol. 27, 255–265.

Menikoff, R., Plohr, B.J., 1989. The Riemann problem for fluid-flow of real materials. Rev. Modern Phys. 61, 75–130.

Mueller, M.E., Blanquart, G., Pitsch, H., 2009. A joint volume-surface model of soot aggregation with the method of moments. Proc. Combust. Inst. 32, 785–792.

Patel, R.G., Desjardins, O., Fox, R.O., 2019. Three-dimensional conditional hyperbolic quadrature method of moments. J. Comp. Phys. X 1, 100006.

Pfister, R., Schwarz, K.A., Janczyk, M., Dale, R., Freeman, J.B., 2013. Good things peak in pairs: a note on the bimodality coefficient. Front. Psychol. 4, 700.

Plesset, M.S., Prosperetti, A., 1977. Bubble dynamics and cavitation. Annu. Rev. Fluid Mech. 9, 145–185.

Preston, A.T., Colonius, T., Brennen, C.E., 2007. A reduced-order model of diffusive effects on the dynamics of bubbles. Phys. Fluids 19, 123302.

Radhakrishnan, A., Le Berre, H., Wilfong, B., Spratt, J.-S., Rodriguez, M., Colonius, T., Bryngelson, S.H., 2024. Method for scalable and performant GPU-accelerated simulation of multiphase compressible flow. Comp. Phys. Comm. 302, 109238.

Schlegel, F., Hänsch, S., Krull, B., Meller, R., Kota, S.P., 2025. Comparison of upper boundary treatments for bubble column simulations with the two-fluid model. Exp. Comput. Multiph. Flow 7, 227–244.

Sibra, A., Dupays, J., Murrone, A., Laurent, F., Massot, M., 2017. Simulation of reactive polydisperse sprays strongly coupled to unsteady flows in solid rocket motors: Efficient strategy using Eulerian multi-fluid methods. J. Comput. Phys. 339, 210–246.

Toro, E., Spruce, M., Speares, W., 1994. Restoration of the contact surface in the HLL-Riemann solver. Shock Waves 4, 25–34.

Vaca-Revelo, D., Wilfong, B., Bryngelson, S.H., Gnanaskandan, A., 2026. Hardware-accelerated phase-averaging for cavitating bubbly flows. Int. J. Multiph. Flow 199, 105674.

Vanni, M., 2000. Approximate population balance equations for aggregation breakage processes. J. Colloid Interface Sci. 221, 143–160.

Vorobyev, M., Lobanov, P., Chinak, A., Kashinsky, O., 2025. Effect of flow direction and capillary orientation on the bubble detachment diameter in liquid cross-flow. Exp. Comput. Multiph. Flow 7, 323–335.

Yuan, C., Fox, R.O., 2011. Conditional quadrature method of moments for kinetic equations. J. Comput. Phys. 230, 8216–8246.

Zhang, D.Z., Prosperetti, A., 1994. Ensemble phase-averaged equations for bubbly flows. Phys. Fluids 6, 2956–2970.